

## Non-invasive high-frequency vascular ultrasound elastography

Roch L Maurice<sup>1</sup>, Michel Daronat<sup>1</sup>, Jacques Ohayon<sup>3</sup>,  
Ékatherina Stoyanova<sup>1</sup>, F Stuart Foster<sup>4</sup> and Guy Cloutier<sup>1,2</sup>

<sup>1</sup> Laboratory of Biorheology and Medical Ultrasonics, Research Center, University of Montreal Hospital, Québec, Canada

<sup>2</sup> Department of Radiology, Radio-oncology and Nuclear Medicine, University of Montreal, Québec, Canada

<sup>3</sup> Laboratory TIMC-IMAG, UMR CNRS 5525, Institut A. Bonniot, 38706 La Tronche, France

<sup>4</sup> Department of Medical Biophysics, Sunnybrook and Women's College Health Sciences Centre, University of Toronto, Ontario, Canada

E-mail: guy.cloutier@umontreal.ca

Received 2 December 2004, in final form 1 February 2005

Published 22 March 2005

Online at [stacks.iop.org/PMB/50/1611](http://stacks.iop.org/PMB/50/1611)

### Abstract

Non-invasive vascular elastography (NIVE) was recently introduced to characterize mechanical properties of superficial arteries. In this paper, the feasibility of NIVE and its applicability in the context of high-frequency ultrasound imaging is investigated. First, experiments were performed *in vitro* on vessel-mimicking phantoms. Polyvinyl alcohol cryogel was used to create two double-layer vessels with different mechanical properties. In both cases, the stiffness of the inner layer was made softer. Radial stress was applied within the lumen of the phantoms by applying incremental static pressure steps with a column of a flowing mixture of water–glycerol. The vessel phantoms were insonified at 32 MHz with an ultrasound biomicroscope to provide cross-section sequences of radio-frequency (RF) ultrasound data. The Lagrangian speckle model estimator (LSME) was used to assess the two-dimensional-strain tensors, and the composite Von Mises elastograms were computed. A new implementation of the LSME based on the optical flow equations was introduced. Deformation parameters were estimated using an inversion algorithm. For each *in vitro* experiment, both layers of approximately 1 mm were distinguished. Second, the use of the method for the purpose of studying small vessels (MicroNIVE) in genetically engineered rodents was introduced. Longitudinal scans of the carotid artery were performed at 40 MHz. The *in vivo* results give confidence in the feasibility of MicroNIVE as a potential tool to non-invasively study the impact of targeted genes on vascular remodelling in rodents.

(Some figures in this article are in colour only in the electronic version)

## 1. Introduction

In the early 1990s, Ophir *et al* (1991) introduced elastography, which is defined as biological tissue elasticity imaging. Primary objectives of elastography were to complement B-mode ultrasound as a screening method to detect hard areas in the breast (Garra *et al* 1997). Within the last few years, elastography has also found application in vessel wall characterization using endovascular catheters (de Korte *et al* 1997, 1998, 2000a, 2000b, Brusseau *et al* 2001). Recently, several groups have proposed different approaches to non-invasively characterize superficial arteries by using standard extra-corporeal array transducers. A method to analyse pulsatile motion of carotid artery plaque from a sequence of RF images was developed by Bang *et al* (2003). They used the standard two-dimensional (2D)-correlation technique to compute a displacement vector map of local areas in consecutive images, from which motion dynamics were quantified. It was suggested that the inhomogeneous motion pattern may induce internal forces that could eventually cause fissures and disruption of the plaque leading to emboli and stroke.

Another strategy to non-invasively characterize the carotid artery was proposed by Kanai *et al* (2003). They developed a novel phased tracking method that divides the arterial wall into multiple layers; dynamic changes in the thickness of each layer during one heartbeat are then measured. Assuming that the arterial wall is incompressible and that the blood pressure is applied perpendicularly to each layer, they proposed to compute a map of elastic moduli. In another study, Mai and Insana proposed to monitor deformations in tissues surrounding superficial arteries (Mai and Insana 2002). A tissue-like gelatin elasticity-flow phantom and *in vivo* scanning of the normal brachial artery were used to validate the method. Finally, a phase-sensitive 2D speckle tracking method was recently proposed to detect renal transplant chronic allograft nephropathy (Weitzel *et al* 2004).

### 1.1. Non-invasive vascular elastography (NIVE)

Our group recently investigated the potential of a new method to non-invasively characterize mechanical properties of superficial arteries; the approach was labelled as NIVE for 'non-invasive vascular elastography' (Maurice *et al* 2004b). Investigating the forward problem for a cross-sectional vessel wall in NIVE, it was shown that motion parameters might be difficult to interpret; that is because tissue motion occurs radially within the vessel wall whereas the ultrasound beam propagates axially. As a consequence of that, the axial and lateral strain parameters<sup>5</sup> are subjected to hardening and softening artefacts<sup>6</sup>, which are to be counteracted to appropriately characterize the vessel wall. With the NIVE approach, the Von Mises coefficient (VM) (SAS IP Inc. 1999, Mase 1970) was proposed as a new parameter to circumvent such mechanical artefacts. The Lagrangian speckle model estimator (LSME), proposed in (Maurice and Bertrand 1999), was used because it provides the full 2D-strain tensor required to compute the VM coefficient.

<sup>5</sup> Most of the conventional methods in elastography only provide the map of the strain distribution in the direction of the ultrasound beam propagation (axial strain, or radial strain in endovascular elastography). Tissue stiffness is conventionally represented with a colour code where dark and bright regions are associated with hard and soft tissues, respectively.

<sup>6</sup> When an elastogram wrongly associates a strain pattern with hard or soft tissues, this is known in the literature as hardening and softening artefacts, respectively. These artefacts are also known as mechanical artefacts and originate from a combination of the intrinsic mechanical properties of the underlying tissue, its geometry and its kinetics.

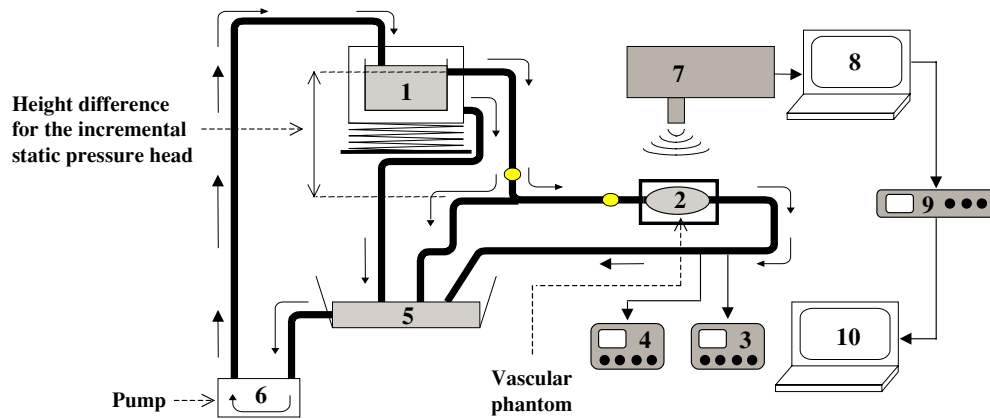


**Figure 1.** Schematic of the experimental set-up: (1) is the top reservoir, (2) the vascular phantom, (3) the electromagnetic flowmeter, (4) the pressure monitor, (5) the bottom reservoir, (6) the peristaltic pump, (7) the scanhead of the ultrasound biomicroscope, (8) the ultrasound biomicroscope, (9) the radio-frequency signal pre-amplifier and (10) the analogue-to-digital acquisition board installed in a computer.

## 1.2. Objectives

Recently, preliminary results from *in vitro* experimentations emphasized the potential of NIVE to characterize the mechanical properties of small vessels (Maurice *et al* 2004c). In the current study, the potential of high-frequency NIVE is further investigated and an improvement of the LSME is proposed. Experiments were conducted on vessel-mimicking phantoms with a small lumen diameter of 1.5 mm and a wall thickness of 2 mm. Preliminary *in vivo* elastograms, acquired over the carotid artery of normotensive and hypertensive rats (MicroNIVE), are also presented.

## 2. Materials

### 2.1. Experimental set-up

Figure 1 gives an overview of the experimental set-up used to produce mechanical deformation of polyvinyl alcohol cryogel (PVA-C) vessel-mimicking phantoms, and the procedure utilized to collect RF ultrasound data that allowed computing vascular elastograms. A mixture of water–glycerol was circulated in the flow phantom. The height difference between the top (1) and bottom reservoirs (5) allowed adjustment of the gravity-driven flow rate and static pressure within the lumen of the phantom (2). A peristaltic pump (6) was used to circulate the fluid from the bottom to the top reservoirs. The flow rate was measured with an electromagnetic flowmeter (Cliniflow II, model FM 701D, Carolina Medical, King, NC, USA; label 3 in figure 1), and the pressure was monitored by a MDE Escort instrument (model E102, Medical Data Electronics, Arleta, Ca, USA; label 4 in figure 1). As illustrated in figure 1, the flow phantom was not directly connected to the tubing of the top reservoir to facilitate the small incremental pressure step adjustments necessary to obtain correlated deformation of the RF signals within the PVA-C vessel wall.

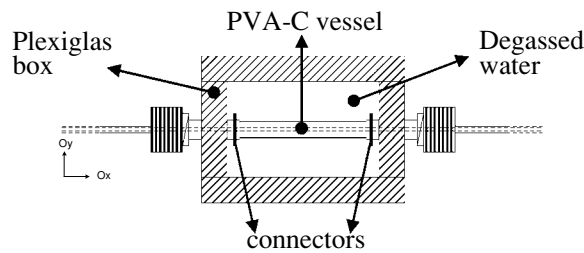


**Figure 2.** Schematic of the vascular flow phantom. The polyvinyl alcohol cryogel (PVA-C) vessel was positioned between two watertight connectors, in a Plexiglas box filled with degassed water at room temperature. Rubber o-rings were used to tighten the PVA-C vessel onto Plexiglas tubes at both extremities.

### 2.2. Vascular phantom (label 2 in figure 1)

As shown in figure 2, the PVA-C vessel of the flow phantom was positioned between two watertight connectors, in a Plexiglas box filled with degassed water at room temperature. Rubber o-rings were used to tighten the PVA-C vessel onto Plexiglas tubes at both extremities.

Based on previous works by Chu and Rutt (1997), the tissue-mimicking vessel was made of PVA-C. This biogel solidifies and acquires its mechanical rigidity by increasing the number of freeze/thaw cycles. Indeed, the number of freeze/thaw cycles modifies the structure of the material by increasing the reticulation of fibres. It was shown that the elastic and acoustic properties of PVA-C are in the range of values found for soft biological tissues (Chu and Rutt 1997). More specifically, the authors demonstrated, in their study, that the stress–strain relationship can be very close to that of a pig aorta.

The vessel-mimicking phantoms approximately had a 1.5 mm lumen diameter, 2 mm wall thickness and 52 mm length. A 1.5% by weight of Sigmacell (type 20, S-3504, Sigma-Aldrich, St-Louis, MO, USA) was added to the PVA-C to provide acoustical scatterers. For this study, two double-layer vessels were constructed. Each layer had a thickness close to 1 mm, and the inner layer was made softer than the outer one. In the first double-layer phantom, the numbers of freeze–thaw cycles were set at 2 and 4 for the inner and the outer portions of the wall, respectively; in the second phantom, the numbers of cycles were set at 1 and 2, respectively. Each freeze–thaw cycle took 24 h and the temperature was incrementally varied from  $-20\text{ }^{\circ}\text{C}$  to  $20\text{ }^{\circ}\text{C}$ , by using a specifically designed electronic controller (Watlow, model 981, Winona, MN, USA) and a freezer equipped with heated elements (Supra Scientifique, model YF-204017, Terrebonne, QC, Canada). Figure 3 shows a schematic representation of both moulds that were used to produce double-layer vessel-mimicking phantoms. At a first instance, PVA-C was poured between the first and second templates; that underwent ( $n_o - n_i$ ) freeze/thaw cycles<sup>7</sup> to provide the external layer. Secondly, fresh PVA-C was poured between the second and third templates, while maintaining the first template in place, which underwent  $n_i$  freeze/thaw cycles to provide a complete double-layer vessel-mimicking phantom.

### 2.3. Animal models

For the purpose of investigating the feasibility of MicroNIVE on small animals, ultrasound RF data were acquired on 6 male rats: 3 normotensive Norway Brun rats (labelled as NT1, NT2 and NT3) and 3 spontaneously hypertensive rats<sup>8</sup> (HT1, HT2 and HT3), respectively.

<sup>7</sup> For the purpose of clarity, we define  $n_i$  and  $n_o$  as the numbers of cycles for the inner and the outer layers, respectively.

<sup>8</sup> The spontaneously hypertensive rats are usually referred to as SHR.

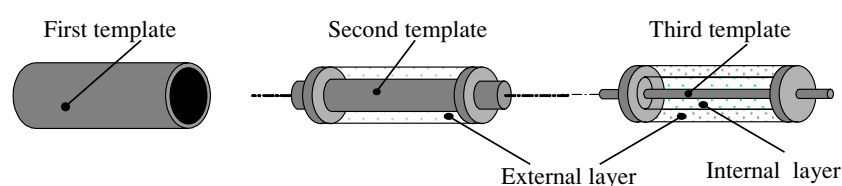


**Figure 3.** Schematic of both moulds that were used to manufacture double-layer PVA-C vessel-mimicking phantoms. The simulated vessels had a 1.5 mm lumen diameter, a 2 mm wall thickness (roughly 1 mm for each layer), and a 52 mm length.

All animals were 15 weeks old and they were anaesthetized by inhalation of 1.5% isoflurane. The body temperature of each animal was monitored with a rectal probe (Thermalert TH-5, Physitemp Instruments, Clifton, NJ, USA) and maintained at  $37 \pm 1$  °C by using a heating surface. The mean systolic pressures for NT and HT rats (measured with a tail-cuff monitoring system, Kent Scientific, model XBP-1000, Torrington, CT, USA) were  $87 \pm 12$  mmHg and  $158 \pm 16$  mmHg, whereas the heart beats were  $323 \pm 15$  beats  $\text{min}^{-1}$  and  $365 \pm 6$  beats  $\text{min}^{-1}$ , respectively. The hairs over the neck were shaved and further removed with a depilatory cream (Nair, Church and Dwight Co., USA). Sequences of RF data were acquired over longitudinal sections of the carotid artery.

#### 2.4. High-frequency imaging systems (labels 7 and 8 in figure 1)

To allow computing vascular elastograms of small vessels, high-resolution ultrasound systems with access to the RF data were required (ultrasound biomicroscope, Visualsonics, VS-40 for *in vitro* data and Vevo 660 for *in vivo* data, Toronto, Canada). The VS-40 was equipped with a single-element oscillating transducer with a central frequency of 32 MHz,  $f$ -number = 2, diameter = 3 mm, focal length = 6 mm, and bandwidth at  $-6$  dB of 110%. As recently reported (Foster *et al* 2002), the axial and lateral resolutions of the instrument can reach  $30 \mu\text{m}$  and  $70 \mu\text{m}$ , respectively. For the purpose of the *in vitro* experiments, a transmit frequency of 40 MHz was used (the frequencies available on the VS-40 system were 19, 25, 40 or 55 MHz) and the frame rate was 8 images  $\text{s}^{-1}$ . The bandpass filter was selected to optimize the bandwidth of the received echoes, and thus the axial resolution. On the other hand, the Vevo 660 is an improved version of the VS-40 ultrasound system. Indeed, it is equipped with an encapsulated oscillating element transducer. The frame rate was also improved to 30 images  $\text{s}^{-1}$ . For the purpose of imaging rats' carotid arteries, a 40 MHz central frequency transducer,  $f$ -number = 2, diameter = 3 mm, focal length = 6 mm, and bandwidth at  $-6$  dB of 110%, was used. The transmit frequency was 40 MHz.

#### 2.5. Acquisition protocol

The ultrasound biomicroscope provides an RF output from which the received RF data were transferred to a pre-amplifier, for *in vitro* experiments only (Panametrics, model 5900 PR, Waltham, MA, USA; label 9 in figure 1). The RF signals from the VS-40 or Vevo 660 system were digitized with an acquisition board (Gagescope, model 8500 CS, Montreal, QC, Canada; label 10 in figure 1) installed in a personal computer. The sampling frequency was 500 MHz, in 8 bit format.

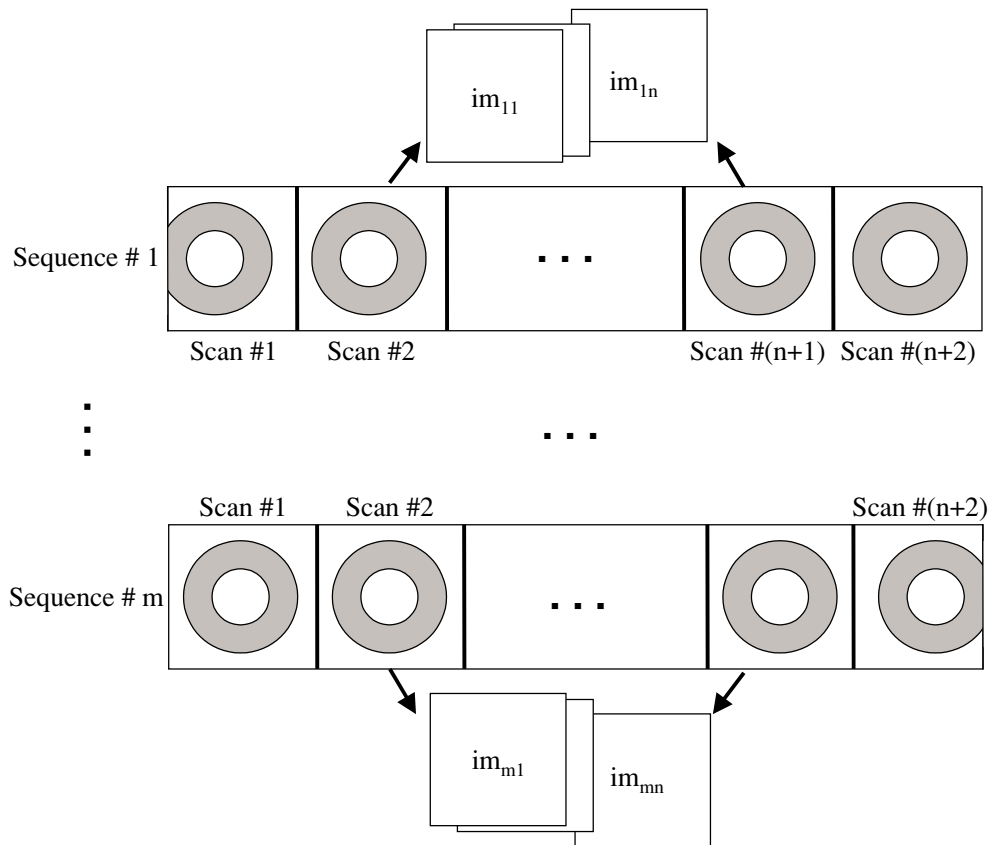


**Figure 4.** Schematic of the data pre-processing. For each of the ' $m$ ' static pressure levels, ' $n + 2$ ' scans (512 RF lines/scan) of the phantom were acquired to provide a 'sequence'. The ' $m$ ' sequences were then partitioned into  $m \times n$  complete images ( $im_{ij}$ ). Following this, image registration was proceeded for the  $im_{ij}$  with respect to  $im_{11}$ , using cross-correlation analysis.

### 2.6. Data pre-processing

Regarding the *in vitro* experiments, ' $n + 2$ ' scans (512 RF lines/scan) of the phantom were acquired at each static pressure to provide a single image; for simplicity, this whole image is labelled as a 'sequence'. The number ' $n + 2$ ' ( $n \geq 1$ ) was chosen only to ensure that at least ' $n$ ' complete scans of the vessel would be available. Indeed, as illustrated in figure 4, the first or/and the last scan in a sequence could be incomplete, since no synchronization of the 8 Hz oscillating element was made available by the instrument. Moreover, it is important to note that because of the back and forth mechanical scanning process, the  $(n + 1)$ th scan has an opposite lateral orientation with the  $n$ th one; that was also compensated for in the pre-processing of the data. Assuming ' $m$ ' pressure steps, ' $m$ ' sequences were then acquired; this is equivalent to ' $m \times (n + 2)$ ' scans of the vessel.

As illustrated in figure 4, the first step of the data pre-processing consisted of extracting ' $n$ ' separate and complete scans from each sequence. For the purpose of clarity, these are labelled as ' $im_{ij}$ ', where ' $i$ ' and ' $j$ ' are associated with the sequence number and the scan position in the sequence, respectively. A set of ' $n$ '  $im_{ij}$ , for each level of pressure, was then available for further processing. In the second step, image registration was proceeded for the  $im_{ij}$  with

respect to  $im_{11}$ , using 2D cross-correlation analysis. This basic process specifically aimed to compensate for some eventual translational motion, which might originate from unwanted movements of the acquisition system and of the experimental apparatus.

Regarding the *in vivo* experiments, the acquired RF data underwent the same pre-processing as presented in figure 4 to extract complete frames of the carotid vessel. The elastograms were computed by considering all successive RF images that were digitized over several cardiac cycles. No averaging was used to display the axial elastograms presented here. Manual segmentation was done to display only the strain patterns within the vascular wall. It is to note that the Von Mises coefficient was not used to display the strain patterns computed with the LSME, because longitudinal sections of the carotid vessels were acquired instead of transverse planes. Because of this, axial elastograms were sufficient since they are not subjected to hardening and softening artefacts (because motions ran quasi-parallel with the ultrasound beam). So far, we do believe that the RF data with the highest correlation between successive frames (i.e., the data shown in the next section) corresponded to measurements performed in diastole, but this would need to be validated with proper synchronization of the ultrasound RF data within the heart cycle. Such synchronization was not available in the current study.

### 3. Methods

The Lagrangian speckle model estimator (LSME), which was used to compute the elastograms, is described in detail elsewhere (Maurice *et al* 2004b). The LSME is a 2D model-based estimator that allows computation of the full 2D-strain tensor (Maurice and Bertrand 1999). The approach relies on a tissue-motion model and on a dynamic image-formation model. The tissue-motion model was adapted here to consider a 3D kinetics; its application to investigate 2D tissue-motion is presented.

#### 3.1. Tissue-motion model

The vascular tissue in mammals and boundary conditions are generally heterogeneous; the vascular wall is thus expected to deform non-uniformly. To assess such tissue motion, the LSME requires subdividing the region of interest (ROI) within the vascular wall into several partitions<sup>9</sup>, for which motion can be assumed as affine. In other words, motion for each partition can be approximated by the zero-order and first-order terms of a Taylor-series expansion. For a 3D tissue, assuming that the origin is set at  $(0, 0, 0)$ , this can be expressed as

$$\begin{bmatrix} x \\ y \\ z \end{bmatrix} = \underbrace{\begin{bmatrix} x(0, 0, 0, t) \\ y(0, 0, 0, t) \\ z(0, 0, 0, t) \end{bmatrix}}_{\text{Tr}} + \underbrace{\begin{bmatrix} \frac{\partial x}{\partial x_0} & \frac{\partial x}{\partial y_0} & \frac{\partial x}{\partial z_0} \\ \frac{\partial y}{\partial x_0} & \frac{\partial y}{\partial y_0} & \frac{\partial y}{\partial z_0} \\ \frac{\partial z}{\partial x_0} & \frac{\partial z}{\partial y_0} & \frac{\partial z}{\partial z_0} \end{bmatrix}}_{\text{LT}}(0,0,0,t) \begin{bmatrix} x_0 \\ y_0 \\ z_0 \end{bmatrix}. \quad (1)$$

Equation (1) defines an affine transformation, i.e., it is the result of a translation (vector [Tr]) and of a linear geometrical transformation of coordinates (matrix [LT]). Equation (1) can also be seen as trajectories that describe a tissue motion in a region of constant strain. Strain is usually defined in terms of the gradient of a displacement field; hence, as  $(x, y, z)$  represents the new position of a point  $(x_0, y_0, z_0)$ , the  $(u, v, w)$  displacement vector in the Cartesian

<sup>9</sup> The partitions are equivalent to the measurement windows. Details on the partitioning process are given in (Maurice *et al* 2004b).

coordinate system is given by

$$\begin{bmatrix} u \\ v \\ w \end{bmatrix} = \begin{bmatrix} x - x_0 \\ y - y_0 \\ z - z_0 \end{bmatrix} = \underbrace{\begin{bmatrix} x(0, 0, 0, t) \\ y(0, 0, 0, t) \\ z(0, 0, 0, t) \end{bmatrix}}_{\text{Tr}} + \Delta \begin{bmatrix} x_0 \\ y_0 \\ z_0 \end{bmatrix}, \quad \text{with}$$

$$\Delta = \underbrace{\begin{bmatrix} \frac{\partial x}{\partial x_0} - 1 & \frac{\partial x}{\partial y_0} & \frac{\partial x}{\partial z_0} \\ \frac{\partial y}{\partial x_0} & \frac{\partial y}{\partial y_0} - 1 & \frac{\partial y}{\partial z_0} \\ \frac{\partial z}{\partial x_0} & \frac{\partial z}{\partial y_0} & \frac{\partial z}{\partial z_0} - 1 \end{bmatrix}}_{\text{LT-1}} \cdot \quad (2)$$

In equation (2), [I] is the three-dimensional (3D) identity matrix. The  $\varepsilon_{ij}$ , which are the components of the 3D-strain tensor  $\varepsilon$ , can then be defined in terms of  $\Delta$  as

$$\varepsilon_{ij}(t) = \frac{1}{2}[\Delta_{ij}(t) + \Delta_{ji}(t)]. \quad (3)$$

Considering the hypothesis that biological soft tissues are weakly compressible (Krouskop *et al* 1987), let us also assume isotropy for each partition. According to that, for a unidirectional ( $y$ ) gradient of compression, the following approximation can be done inside a given partition:

$$\text{tr}(\varepsilon) = 0, \quad \text{i.e.} \quad \varepsilon_{xx} = \varepsilon_{zz} \cong -\frac{\varepsilon_{yy}}{2}. \quad (4)$$

In equation (4),  $\text{tr}(\cdot)$  defines the trace of a matrix, and  $\varepsilon_{yy}$  ( $=\Delta_{yy}$ ) gives the axial strain. In the case where longitudinal images of the vessels are studied,  $\varepsilon_{yy}$  may be sufficient to characterize the wall in MicroNIVE. On the other hand, to counteract mechanical artefacts of cross-sectional images, the Von Mises (VM) coefficient (SAS IP Inc. 1999, Mase 1970) was recently proposed as a new characterization parameter (Maurice *et al* 2004b) since it is independent of the orientation. Knowing the strain tensor given by equation (3), the 2D VM coefficient can be computed; it is mathematically expressed as

$$\xi = \sqrt{\varepsilon_{xx}^2 + \varepsilon_{yy}^2 - \varepsilon_{xx}\varepsilon_{yy} + 3\varepsilon_{xy}^2} = \sqrt{\Delta_{xx}^2 + \Delta_{yy}^2 - \Delta_{xx}\Delta_{yy} + \frac{3}{4}(\Delta_{xy} + \Delta_{yx})^2}. \quad (5)$$

In practice, a 3D ROI is investigated in NIVE or MicroNIVE whereas 2D images are currently used to assess tissue motion. Owing to this, the 2D VM parameter ( $\xi$ ) should take into account equation (4). Accordingly, equation (5) can be rewritten as

$$\xi = \sqrt{\frac{7}{4}\varepsilon_{yy}^2 + 3\varepsilon_{xy}^2} = \frac{1}{2}\sqrt{7\Delta_{yy}^2 + 3(\Delta_{xy} + \Delta_{yx})^2}. \quad (6)$$

### 3.2. The Lagrangian speckle model estimator (LSME)

Assuming a small ROI and small tissue motion, the LSME can mathematically be formulated as finding the  $\text{LT}_{2\text{D}}$  that minimizes the objective function  $f$  given as

$$f = \|I(x, y, t) - I(x, y, t + dt)_{\text{LT}_{2\text{D}}}\|^2 = \|I(x, y, t) - I_{\text{Lag}}(x, y, t + dt)\|^2, \quad (7)$$

where  $(x, y)$  defines the image coordinate system, and ' $t$ ' indicates the time.  $I(x, y, t)$  is the pre-tissue-motion RF image,  $I(x, y, t + dt)$  is the post-tissue-motion RF image, and  $I_{\text{Lag}}(x, y, t + dt)$  is the Lagrangian speckle image (LSI). It is worth mentioning that the LSI was defined as a post-tissue-motion RF image  $I(x, y, t + dt)$  that was numerically compensated for tissue motion, so as to achieve the best match with  $I(x, y, t)$  (Maurice and Bertrand 1999). The appellation 'Lagrangian' refers to the Lagrangian description of motion. The minimum

of equation (7) was obtained by using the appropriate [LT<sub>2D</sub>], a 2D linear transformation matrix<sup>10</sup>.

### 3.3. Implementation of the LSME

In previous applications of the LSME (Maurice *et al* 2004a, 2004b, 2004c, 2005, Maurice and Bertrand 1999), equation (7) was numerically solved with an iterative procedure, using the regularized nonlinear minimization method of Levenberg–Marquardt. In this paper, a new implementation of the LSME is proposed. It is based on the assumption that, for small tissue motion, the scatterers (cellular components of the vessel) conserve on average their acoustical properties and then speckle can be seen as a material property. Accordingly, an optical flow-based algorithm was developed. The relationship between speckle and optical flow equations (Horn 1986) is presented here.

**3.3.1. The optical flow equations.** The material derivative of a function  $I(x, y, t)$  is given as

$$\frac{dI}{dt} = I_x \frac{dx}{dt} + I_y \frac{dy}{dt} + I_t, \quad (8)$$

with  $I_x$ ,  $I_y$  and  $I_t$  being the partial derivatives of  $I(x, y, t)$  with respect to  $x$ ,  $y$  and  $t$ , respectively. Here,  $I_t$  is the time rate of change of  $I(x, y, t)$  in the observer coordinate system,  $(\frac{dx}{dt}, \frac{dy}{dt})$  is the velocity vector of a ‘material point’ located at  $(x, y)$ , and  $\frac{dI}{dt}$  is the intrinsic rate of change of the material point. For a time sequence of two images at an interval  $dt$ , equation (8) can be rewritten as

$$dI = I_x dx + I_y dy + (I(x, y, t + dt) - I(x, y, t)). \quad (9)$$

Here,  $(dx, dy)$  represents the displacement vector of the ‘material point’ located at  $(x, y)$  in the time interval  $dt$ .

Furthermore, assuming speckle being a material property that is preserved with motion ( $dI(x, y, t) = 0$ ), and assuming  $I(x, y, t + dt)$  (equivalently,  $I_{\text{Lag}}(x, y, t + dt)$ ) being a very close approximation of  $I(x, y, t)$ , one obtains

$$I_x dx + I_y dy = -(I_{\text{Lag}}(x, y, t + dt) - I(x, y, t)). \quad (10)$$

Now, with respect to equations (2) and (3), equation (10) can be rewritten as

$$\begin{aligned} I_x u + I_y v &= -(I_{\text{Lag}}(x, y, t + dt) - I(x, y, t)) \\ \therefore (t_x + \Delta_{11}x + \Delta_{12}y)I_x + (t_y + \Delta_{21}x + \Delta_{22}y)I_y &= -\tilde{I}_t. \end{aligned} \quad (11)$$

For the purpose of clarity, the following simplifications can be made in equation (11):

$$t_x = x(0, 0, t) \quad t_y = y(0, 0, t) \quad \text{and} \quad \tilde{I}_t = (I_{\text{Lag}}(x, y, t + dt) - I(x, y, t)).$$

Finally, if the ROI has a size of  $p \times q$  pixels, the discrete form of equation (11) can be written as

$$\begin{bmatrix} I_{x_1} x_1 & I_{x_1} y_1 & I_{x_1} & I_{y_1} x_1 & I_{y_1} y_1 & I_{y_1} \\ I_{x_2} x_2 & I_{x_2} y_2 & I_{x_2} & I_{y_2} x_2 & I_{y_2} y_2 & I_{y_2} \\ \vdots & \vdots & \vdots & \vdots & \vdots & \vdots \\ \vdots & \vdots & \vdots & \vdots & \vdots & \vdots \\ I_{x_{p \times q}} x_{p \times q} & I_{x_{p \times q}} y_{p \times q} & I_{x_{p \times q}} & I_{y_{p \times q}} x_{p \times q} & I_{y_{p \times q}} y_{p \times q} & I_{y_{p \times q}} \end{bmatrix} \begin{bmatrix} \Delta_{11} \\ \Delta_{12} \\ t_x \\ \Delta_{21} \\ \Delta_{22} \\ t_y \end{bmatrix} = - \begin{bmatrix} \tilde{I}_{t_1} \\ \tilde{I}_{t_2} \\ \vdots \\ \vdots \\ \tilde{I}_{t_{p \times q}} \end{bmatrix}. \quad (12)$$

<sup>10</sup> [LT<sub>2D</sub>] can be deduced from [LT]. Indeed, regarding equation (1), [LT<sub>2D</sub>] is defined as a  $2 \times 2$  sub-matrix of [LT]; it is given by the first 2 lines and the first 2 columns of [LT], that is for  $z = z_0 = 0$ .

Solving equation (12) provides  $\Delta$ ,  $t_x$  and  $t_y$  for each pixel of the ROI. One hypothesis supporting equation (12) was that  $dI(x, y, t) = 0$ , i.e., the intensity of each pixel remained the same following tissue motion. In practice, however, because of signal decorrelation, this is rarely the case. Equation (12) then provides a solution for the minimization problem given in equation (7). The main advantage of this method over the previous iterative one (Maurice *et al* 2004a, 2004b, 2004c, 2005, Maurice and Bertrand 1999) is relative to the processing time. Indeed, the computation time is improved by a factor close to 25. Moreover, it is important to note, in this implementation of the LSME, that the motion compensation process providing  $I_{\text{Lag}}(x, y, t + dt)$  is computed using cross-correlation analysis.

#### 4. Results

The double-layer vessel-mimicking phantoms measured 5.5 mm in outer diameter, whereas the RF images extended to 8 mm  $\times$  8 mm. Measurement windows (partitions or ROI) required for the LSME were of 272  $\mu\text{m}$   $\times$  312  $\mu\text{m}$  (200 samples  $\times$  20 RF lines), with 85% axial and lateral overlaps. The estimated motion parameters were post-processed using a 5  $\times$  5 kernel Gaussian filter. Regarding the *in vivo* experiments, the measurement windows were set at 108  $\mu\text{m}$   $\times$  312  $\mu\text{m}$  (80 samples  $\times$  20 RF lines), with 90% axial and lateral overlaps. The estimated axial motion was post-processed using a 1  $\times$  1 kernel Gaussian filter.

##### 4.1. The 2–4 cycles double-layer phantom

For this phantom, the inner layer was softer and underwent two freeze–thaw cycles, whereas the outer one was harder with four freeze–thaw cycles. Following data pre-processing (see figure 4), two sequences of four complete RF images were available. The pressure pre-load was 10 mmHg, and the pressure gradient was 5 mmHg between both sequences. Figure 5(a) shows a B-mode pre-motion image (at 10 mmHg).

To ensure the reproducibility of the method, VM elastograms (equation (6)) were computed comparing  $im_{1j}$  and  $im_{2j}$  ( $j = 1, 2, 3, 4$ ). Figure 5(b) presents an average of four such elastograms that show the visibility of both layers. However, some artefacts are observed in the outer layer. Figure 5(c) plots an average of five axial lines chosen in the middle of the VM elastogram (around  $x = 0$ ). Both layers can quantitatively be differentiated, specifically at the upper side of the vessel (left side of panel (c)) where maximum strains around 0.8% and 0.4% are observed for the inner and the outer layers, respectively.

##### 4.2. The 1–2 cycles double-layer phantom

This second experimentation was performed under the same conditions as for the phantom made of 2–4 freeze–thaw cycles. The intraluminal pressure was increased from 10 mmHg to 40 mmHg with steps of 5 mmHg. We report here results for the following pressure steps: 10–15 mmHg, 15–20 mmHg, 25–30 mmHg and 35–40 mmHg. In each case, four elastograms were averaged for each pressure step to provide the results illustrated in figure 6. On each panel, both layers can be seen and the same strain pattern is observed, with a maximum close to 1.8%. As it could be expected, higher strain values were measured in comparison with the 2–4 freeze–thaw cycles PVA-C study, due to the use of a more compliant phantom.

##### 4.3. Preliminary *in vivo* validation of MicroNIVE

We report here preliminary *in vivo* results on carotid arteries of rats. Figure 7 (panels (a) and (b)) shows two B-mode images obtained for a normotensive rat (NT1) and a hypertensive one

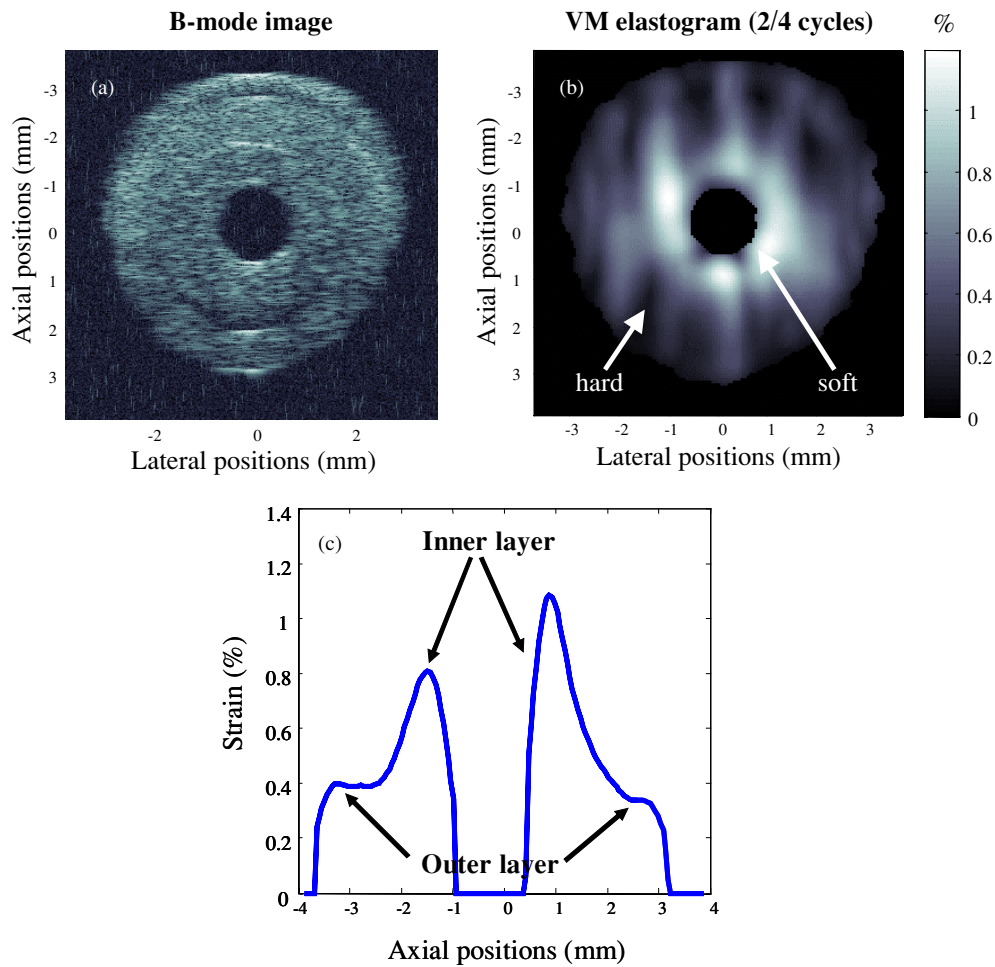


**Figure 5.** (a) Pre-motion B-mode image (RF images were processed to achieve tissue motion); (b) Von Mises elastogram ( $\xi$ ) computed with the Lagrangian speckle model estimator; (c) plot of an average of five axial lines chosen in the middle of  $\xi$  (around  $x = 0$ ).

(HT1), respectively. In both cases, the internal diameter of the carotid was around 1.1 mm, whereas the wall thickness was close to 160  $\mu\text{m}$  for NT1 and 120  $\mu\text{m}$  for HT1, respectively. Panels (c)–(h) of figure 7 show axial strain elastograms computed with the LSME; the colour bar gives the strain in percentage. The negative strains are indicative of vessel dilation (diastolic phase). For most rats, it was difficult to have longitudinal sections of 6 mm, consequently only portions of the carotids are displayed on the elastograms. The carotids of the three normotensive rats (NT1, NT2 and NT3) appear on average twice softer (strain values up to 7%) than those of the hypertensive ones (HT1, HT2 and HT3), where a maximum of 3.3% strain was estimated.

## 5. Discussion

Experiments were first performed *in vitro* on two double-layer vessel-mimicking phantoms of 2–4 and 1–2 freeze–thaw PVA-C cycles, respectively. Radial stress was induced within

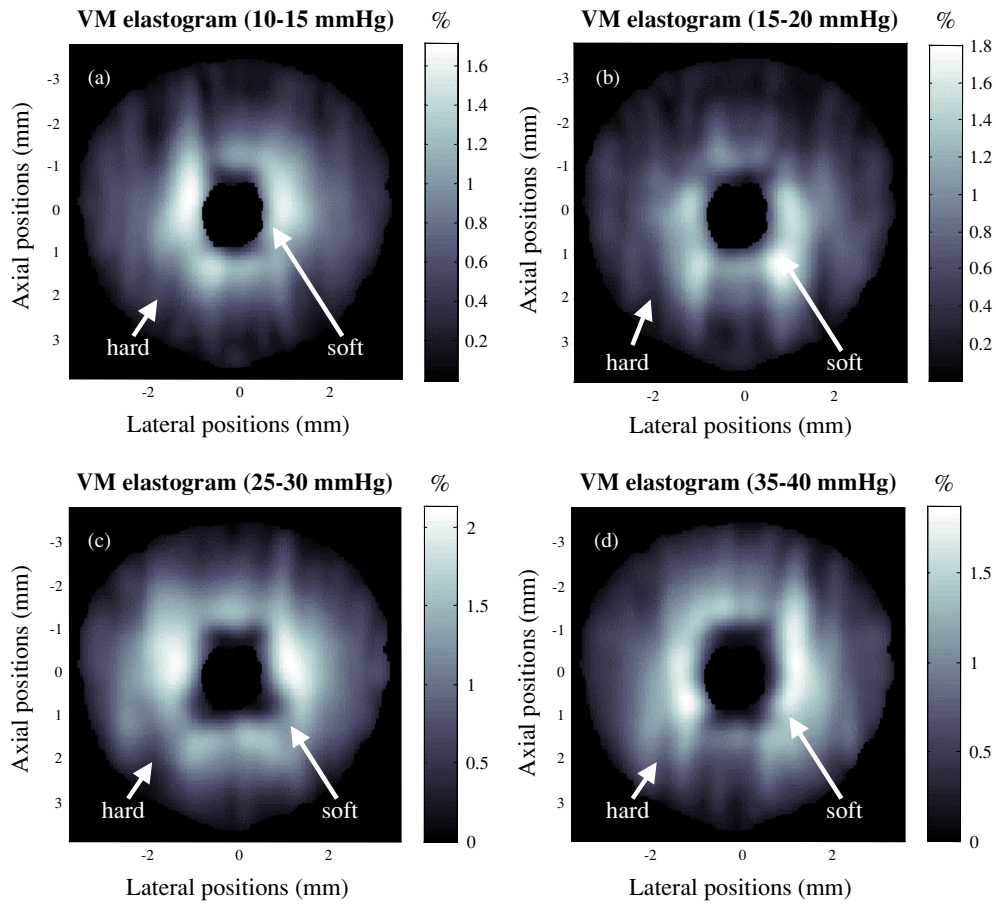


**Figure 6.** (a)–(d): Von Mises elastograms ( $\xi$ ) computed with the Lagrangian speckle model estimator for pressure steps of 10–15 mmHg, 15–20 mmHg, 25–30 mmHg and 35–40 mmHg, respectively.

the lumen of the phantoms by applying incremental static pressure steps with a column of a flowing mixture of water–glycerol. RF data were acquired using a high-resolution ultrasound system, equipped with a 32 MHz transducer. The Von Mises elastograms were then computed using the Lagrangian speckle model estimator (LSME). A new implementation of the LSME was introduced. Under the assumption that speckle behaves as a material property, the optical flow equations were derived to improve the processing time by a factor close to 25.

As shown by equations (5) and (6), the composite VM elastogram requires the four components of the deformation matrix to be computed. Whereas the LSME provides very accurate axial deformation estimates, lateral motion assessment remains a non-trivial problem, due to the relatively limited lateral resolution of RF images. In the current paper, this difficulty was partially circumvented compared to previous attempts (Maurice *et al* 2004c). Indeed, under the assumptions of weak compressibility of biological soft tissues and isotropy inside each measurement window, the lateral strain ( $\varepsilon_{xx} = \Delta_{xx}$ ) was deduced from the axial strain ( $\varepsilon_{yy} = \Delta_{yy}$ ) in equation (4).

Whereas the VM elastograms displayed in figures 5 and 6 showed two visible concentric layers, some artefacts were observed specifically in the outer layer. A potential explanation

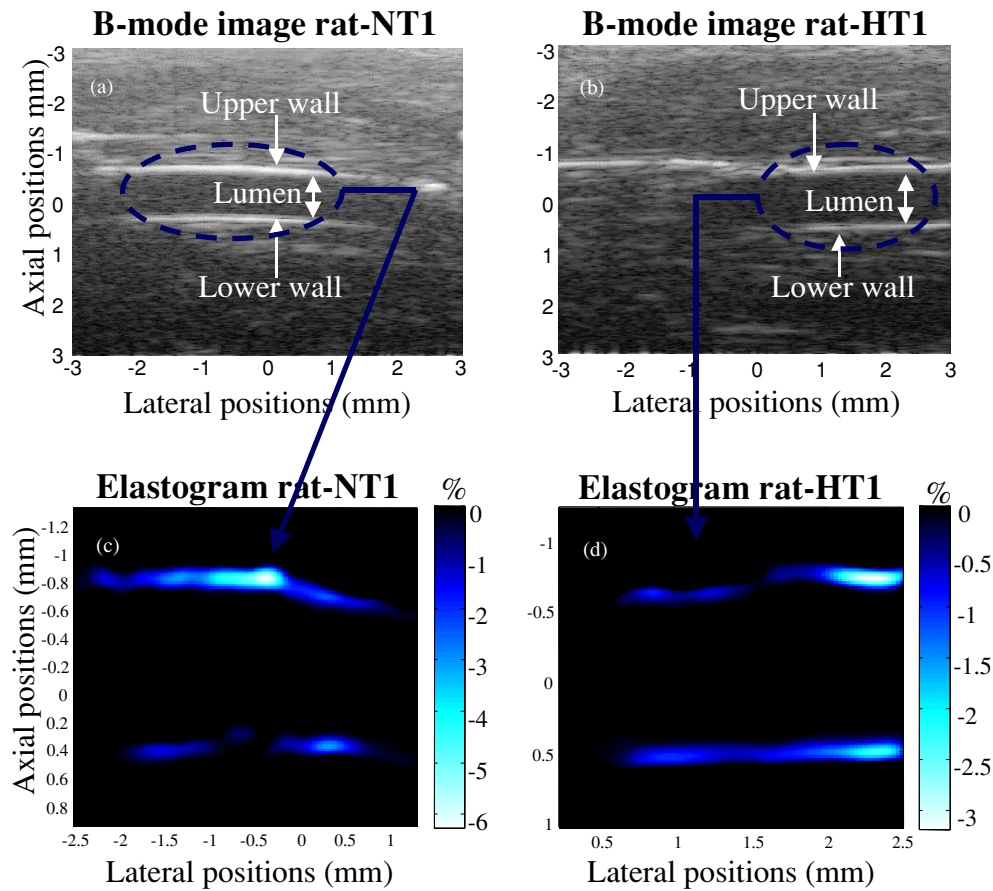


**Figure 7.** (a)–(b): Examples of B-mode images acquired for rats NT1 and HT1, respectively. (c), (e), (g): Elastograms computed for normotensive rats NT1, NT2 and NT3 respectively. (d), (f), (h): Elastograms computed for hypertensive rats HT1, HT2 and HT3 respectively. The carotid arteries of the NTs deform twice than those of the HTs even if the mean systolic pressure was lower ( $87 \pm 12$  mmHg for NTs and  $158 \pm 16$  mmHg for HTs).

to that stems from the fact that an oscillating external single-element transducer was used to acquire the RF data with the VS-40 system. Since a small intraluminal pressure gradient was applied to dilate the vessel-mimicking phantoms, vibrations generated by the rapid oscillating movement of the transducer might have interfered with the RF signals to induce decorrelation noise between pre- and post-motion RF images. This drawback becomes very important specifically in regions of low strains such as the outer layer. This potential problem is expected to be solved with the use of the Vevo 660 system equipped with an encapsulated transducer.

### 5.1. Theoretical prediction of the strain distribution within a concentric axisymmetrical double-layer vessel

In a recent study (Maurice *et al* 2004b), we analytically solved the mechanical problem of a concentric double-layer incompressible and isotropic vessel (vessel embedded in a finite

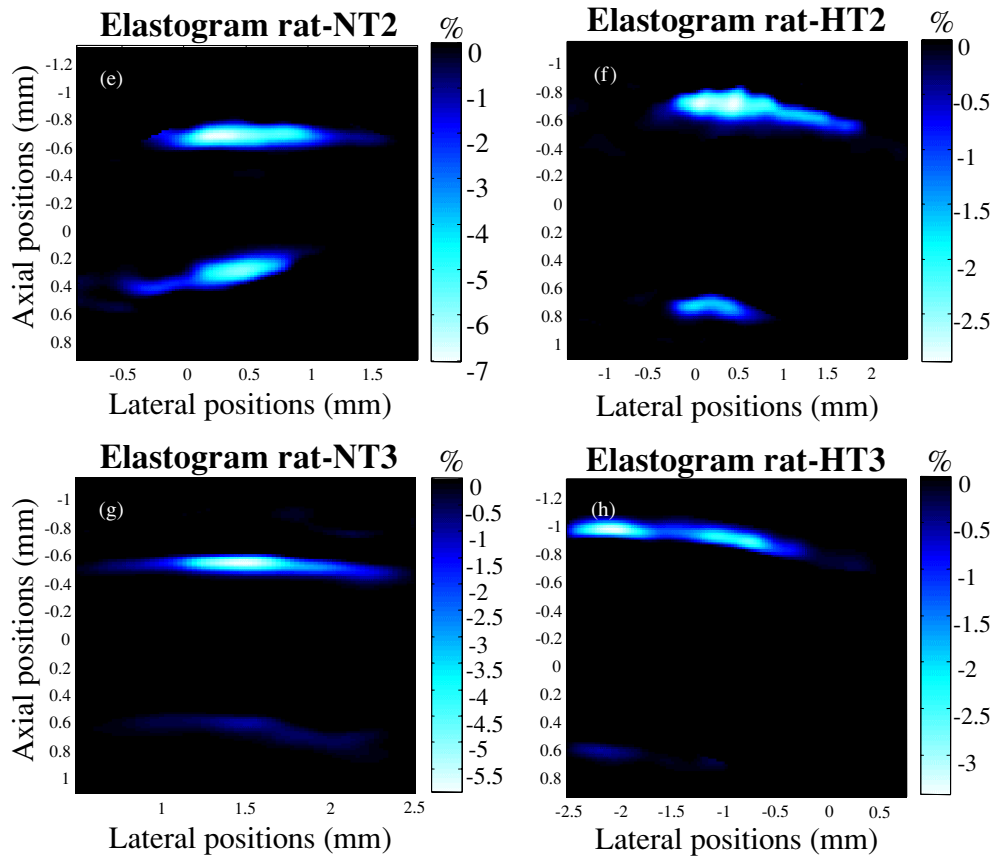


Figure 7. (continued.)

medium). According to equations (A.13)–(A.15) of Maurice *et al* (2004b) reported below as equation (13), no discontinuities were noted in the strain tensor at the interface between both layers of the materials:

$$\begin{aligned}
 \varepsilon_{xx}(x, y) &= \frac{\partial u_x}{\partial x} = K_\infty \frac{y^2 - x^2}{(x^2 + y^2)^2} \\
 \varepsilon_{yy}(x, y) &= \frac{\partial u_y}{\partial y} = K_\infty \frac{x^2 - y^2}{(x^2 + y^2)^2} \\
 \varepsilon_{xy}(x, y) &= \frac{1}{2} \left( \frac{\partial u_x}{\partial y} + \frac{\partial u_y}{\partial x} \right) = -2K_\infty \frac{xy}{(x^2 + y^2)^2}.
 \end{aligned} \tag{13}$$

This suggests that the elastogram of an incompressible double-layer phantom would not allow dissociating both layers, as it was observed in figures 5 and 6. We derived, in the appendix of the current study, the analytical strain tensor for a compressible double-layer thick-wall cylindrical vessel, embedded in an infinite medium and subjected to an intraluminal pressure. Looking at equations (A.19)–(A.21), it is observed that the spatial distribution of the strain components has discontinuities at the layer interfaces. The results of figures 5 and 6 can thus partially be explained by considering PVA-C as a weakly compressible material. However, we do believe that other technical factors contributed to the strain patterns of figures 5 and 6.

For instance, it was difficult to make the PVA-C layers perfectly cylindrical because the recurrent freeze–thaw cycles slightly deformed the vessels. In addition, we probably had a non-slip condition between both layers because the fabrication process, illustrated in figure 3, required two subsequent steps for pouring PVA-C within the first and second templates. These technical conditions may have amplified discontinuities and the visual dissociation between both layers on the elastograms.

### 5.2. Preliminary *in vivo* validation of MicroNIVE

We also reported, in this study, preliminary *in vivo* results on carotid arteries of rats. The wall thickness of those vessels was as small as  $120\ \mu\text{m}$  for HT1. The carotids of the normotensive rats were shown on average twice softer than those of the hypertensive ones. To provide a more rigorous interpretation of these data, one should consider the pressure gradient between the pre-compression and post-compression RF images used to compute those elastograms. This pressure gradient was higher for HT than NT rats, but unfortunately the exact values are not known because the RF images were acquired without any ECG or pressure synchronization.

## 6. Conclusion

This paper addressed the feasibility of non-invasive vascular elastography (NIVE) and its applicability using high-frequency ultrasound for the ultimate goal of investigating the mechanical properties of small vessels (MicroNIVE). Experiments were performed *in vitro* on two double-layer vessel-mimicking phantoms with different mechanical properties. The Lagrangian speckle model estimator (LSME) was used to assess the 2D-strain tensors, allowing computing the composite Von Mises elastograms. The double layers were visible for both phantoms. Moreover, preliminary *in vivo* results on the carotid arteries of rats provided additional confidence in the feasibility of MicroNIVE as a potential tool to non-invasively study the impact of targeted genes on vascular remodelling and plaque development in rodents. MicroNIVE could also be of value to investigate superficial small vessels in humans. Nevertheless, we are aware that more experiments are needed to demonstrate the full potential of MicroNIVE.

## Acknowledgments

This work was supported by grants from the Natural Sciences and Engineering Research Council of Canada (no 138570-01) and Valorisation-Recherche Québec (structuring group program). Dr Cloutier is recipient of a National Scientist award from the Fonds de la Recherche en Santé du Québec. The ultrasound biomicroscopes used in this study were purchased through the support of the Foundation of the University of Montreal Hospital.

## Appendix. Multi-layer thick-wall cylindrical blood vessel embedded in a finite (or infinite) medium: solution for compressible layers

Exact solutions of a pressurized composite thick-wall finite cylinder (composed of  $n$  coaxial layers) of inner and outer radii  $R_{(0)}$  and  $R_{(n)}$  respectively, embedded in an elastic coaxial cylindrical medium of radius  $R_{(n+1)}$ , can be found in linear elasticity assuming that all layers are either incompressible or compressible. Because the mechanical solution for incompressible materials was reported in Maurice *et al* (2004b), we here derive the solution for compressible media.

For the mathematical formulation, the cylindrical and Cartesian unit base vectors and their associated physical coordinates are noted:  $(\vec{e}_r, \vec{e}_\varphi, \vec{e}_z)$ ,  $(\vec{e}_x, \vec{e}_y, \vec{e}_z)$  and  $(r, \varphi, z)$ , and  $(x, y, z)$ , respectively. In the current theoretical appendix, 'i' denotes the layer considered and  $0 \leq \varphi \leq 2\pi$ . For the multi-layer vascular wall,  $1 \leq i \leq n$  and  $R_{(0)} \leq r \leq R_{(n)}$ . For the surrounding tissue,  $i = n + 1$  and  $R_{(n)} \leq r \leq R_{(n+1)}$ . The stress and strain tensors associated with each medium 'i' are denoted as  $[\sigma]^{(i)}$  and  $[\varepsilon]^{(i)}$ , respectively.

The assumption of plane strain was made (in the  $(r, \varphi)$ -plane) because the vessel length is at least of the same order of magnitude as its radial dimension. Neglecting gravity and inertial forces, the stress tensors must satisfy the local equilibrium equations:

$$\nabla \cdot [\sigma]^{(i)} = \vec{0} \quad \text{in} \quad R_{(i-1)} \leq r \leq R_{(i)}, \quad \text{with} \quad i = 1, \dots, n+1. \quad (\text{A.1})$$

Additionally, the displacement fields  $\vec{u}^{(i)}$  as well as the stress tensors  $[\sigma]^{(i)}$  must satisfy the following boundary conditions: the blood pressure  $P_b$  is uniform,

$$[\sigma]^{(1)} \vec{e}_r = -P_b \vec{e}_r \quad \text{at} \quad r = R_{(0)}, \quad (\text{A.2})$$

no stresses are applied on the external surface of the surrounding tissue,

$$[\sigma]^{(n+1)} \vec{e}_r = \vec{0} \quad \text{at} \quad r = R_{(n+1)}, \quad (\text{A.3})$$

and at the vessel layer interfaces as well as between the vessel wall and the surrounding tissue, we must have the continuity of displacement fields and equality of the stress vectors,

$$\vec{u}^{(i)} = \vec{u}^{(i+1)} \quad \text{at} \quad r = R_{(i)}, \quad \text{with} \quad i = 1, \dots, n, \quad (\text{A.4})$$

and

$$[\sigma]^{(i)} \vec{e}_r = [\sigma]^{(i+1)} \vec{e}_r \quad \text{at} \quad r = R_{(i)}, \quad \text{with} \quad i = 1, \dots, n. \quad (\text{A.5})$$

Due to the axisymmetries of the boundary conditions, to the material properties and to the geometry, we are looking for displacement fields  $\vec{u}^{(i)}$  of the following form:

$$\vec{u}^{(i)} = u_r^{(i)}(r) \vec{e}_r \quad \text{in} \quad R_{(i-1)} \leq r \leq R_{(i)}, \quad \text{with} \quad i = 1, \dots, n+1. \quad (\text{A.6})$$

Because all the elastic media are assumed to be compressible and isotropic, they are described by the following constitutive laws,

$$[\sigma]^{(i)} = \lambda^{(i)} \text{div}(\vec{u}^{(i)}) [I] + 2\mu^{(i)} [\varepsilon]^{(i)} \quad \text{in} \quad R_{(i-1)} \leq r \leq R_{(i)}, \quad \text{with} \quad i = 1, \dots, n+1, \quad (\text{A.7})$$

where  $(\lambda^{(i)}, \mu^{(i)})$  are the Lamé coefficients that are related to the Poisson ratios  $\nu^{(i)}$  and Young moduli  $E^{(i)}$  (Findley *et al* 1989):

$$\lambda^{(i)} = \frac{E^{(i)} \nu^{(i)}}{(1 + \nu^{(i)})(1 - 2\nu^{(i)})} \quad \mu^{(i)} = \frac{E^{(i)}}{2(1 + \nu^{(i)})} \quad \text{in} \quad R_{(i-1)} \leq r \leq R_{(i)},$$

with  $i = 1, \dots, n+1$ . (A.8)

The conditions of local equilibrium (equation (A.1)) may be written in terms of the displacement vectors:

$$\text{div}(\vec{u}^{(i)}) = 2A^{(i)} \quad \text{in} \quad R_{(i-1)} \leq r \leq R_{(i)}, \quad \text{with} \quad i = 1, \dots, n+1, \quad (\text{A.9})$$

where  $A^{(i)}$  ( $i = 1, \dots, n+1$ ) are  $n+1$  constants. The factor '2' in equation (A.9) is introduced for commodity reason. From equations (A.9) and (A.6), one can derive the radial displacement solution in each layer,

$$u_r^{(i)}(r) = A^{(i)} r + \frac{B^{(i)}}{r} \quad \text{in} \quad R_{(i-1)} \leq r \leq R_{(i)}, \quad \text{with} \quad i = 1, \dots, n+1, \quad (\text{A.10})$$

where  $B^{(i)}$  ( $i = 1, \dots, n+1$ ) are  $n+1$  additional constants. To determine the  $2(n+1)$  constants ( $A^{(i)}$  and  $B^{(i)}$ ,  $i = 1, \dots, n+1$ ), we have to solve the linear system of  $2(n+1)$  equations given by equations (A.2)–(A.5).

In the particular case of a cylinder made of two layers ( $n = 2$ ) and embedded in a finite medium, the values of the six constants  $A^{(i)}$  and  $B^{(i)}$  ( $i = 1, 2, 3$ ) are obtained by solving the following linear system,

$$R_{(1)}^2 A^{(1)} + B^{(1)} - R_{(1)}^2 A^{(2)} - B^{(2)} = 0, \quad (\text{A.11})$$

$$R_{(2)}^2 A^{(2)} + B^{(2)} - R_{(2)}^2 A^{(3)} - B^{(3)} = 0, \quad (\text{A.12})$$

$$X^{(1)} R_{(1)}^2 A^{(1)} - 2\mu^{(1)} B^{(1)} - X^{(2)} R_{(1)}^2 A^{(2)} + 2\mu^{(2)} B^{(2)} = 0, \quad (\text{A.13})$$

$$X^{(2)} R_{(2)}^2 A^{(2)} - 2\mu^{(2)} B^{(2)} - X^{(3)} R_{(2)}^2 A^{(3)} + 2\mu^{(3)} B^{(3)} = 0, \quad (\text{A.14})$$

$$X^{(1)} R_{(0)}^2 A^{(1)} - 2\mu^{(1)} B^{(1)} = -P_b R_{(0)}^2, \quad (\text{A.15})$$

$$X^{(3)} R_{(3)}^2 A^{(3)} - 2\mu^{(3)} B^{(3)} = 0, \quad (\text{A.16})$$

where  $X^{(i)} = 2(\lambda^{(i)} + \mu^{(i)})$ . The solution when the surrounding tissue is infinite ( $R_{(n+1)} = R_{(3)} \rightarrow \infty$ ) may then be derived from the limits  $A_{\infty}^{(i)} = \lim_{R_{(3)} \rightarrow \infty} A^{(i)}$  and  $B_{\infty}^{(i)} = \lim_{R_{(3)} \rightarrow \infty} B^{(i)}$  ( $i = 1, 2, 3$ ). The Cartesian components of the displacement vectors and strain tensors are then given in the domains  $R_{(i-1)} \leq r \leq R_{(i)}$  with  $i = 1, 2, 3$  by

$$u_x^{(i)}(x, y) = \left( A_{\infty}^{(i)} + \frac{B_{\infty}^{(i)}}{x^2 + y^2} \right) x, \quad (\text{A.17})$$

$$u_y^{(i)}(x, y) = \left( A_{\infty}^{(i)} + \frac{B_{\infty}^{(i)}}{x^2 + y^2} \right) y, \quad (\text{A.18})$$

$$\varepsilon_{xx}^{(i)}(x, y) = \frac{\partial u_x^{(i)}}{\partial x} = A_{\infty}^{(i)} + B_{\infty}^{(i)} \frac{y^2 - x^2}{(x^2 + y^2)^2}, \quad (\text{A.19})$$

$$\varepsilon_{yy}^{(i)}(x, y) = \frac{\partial u_y^{(i)}}{\partial y} = A_{\infty}^{(i)} - B_{\infty}^{(i)} \frac{y^2 - x^2}{(x^2 + y^2)^2}, \quad (\text{A.20})$$

$$\varepsilon_{xy}^{(i)}(x, y) = \frac{1}{2} \left( \frac{\partial u_x^{(i)}}{\partial y} + \frac{\partial u_y^{(i)}}{\partial x} \right) = -2B_{\infty}^{(i)} \frac{xy}{(x^2 + y^2)^2}, \quad (\text{A.21})$$

Interestingly, the solution shows, due to the compressibility of the continuous layers, that the spatial distributions of the strain components have discontinuities at the layer interfaces.

## References

- Bang J, Dahl T, Bruinsma A, Kaspersen J H, Hernes T A N and Myhre H O 2003 A new method for analysis of motion of carotid plaques from RF ultrasound images *Ultrasound Med. Biol.* **29** 967–76
- Brusseau E, Fromageau J, Finet G, Delachartre P and Vray D 2001 Axial strain imaging of intravascular data: results on polyvinyl alcohol cryogel phantoms and carotid artery *Ultrasound Med. Biol.* **27** 1631–42
- Chu K C and Rutt B K 1997 Polyvinyl alcohol cryogel: an ideal phantom material for MR studies of arterial flow and elasticity *Magn. Reson. Med.* **37** 314–9
- de Korte C L, Céspedes E I, Van der Steen A F W and Lancée C T 1997 Intravascular elasticity imaging using ultrasound—Feasibility studies in phantoms *Ultrasound Med. Biol.* **23** 735–46
- de Korte C L, Pasterkamp G, Van der Steen A F W, Woutman H A and Bom N 2000a Characterization of plaque components with intravascular ultrasound elastography in human femoral and coronary arteries *in vitro Circulation* **102** 617–23

- de Korte C L, Van der Steen A F W, Céspedes E I and Pasterkamp G 1998 Intravascular ultrasound elastography in human arteries: initial experience *in vitro* *Ultrasound Med. Biol.* **24** 401–8
- de Korte C L, Van der Steen A F W, Céspedes E I, Pasterkamp G, Carlier S G, Mastik F, Schoneveld A H, Serruys P W and Bom N 2000b Characterization of plaque components and vulnerability with intravascular ultrasound elastography *Phys. Med. Biol.* **45** 1465–75
- Findley W N, Lai J S and Onaran K 1989 *Creep and Relaxation of Nonlinear Viscoelastic Materials* 2nd edn (New York: Dover) pp 46–7
- Foster F S *et al* 2002 A new ultrasound instrument for *in vivo* microimaging of mice *Ultrasound Med. Biol.* **28** 1165–72
- Garra B S, Céspedes E I, Ophir J, Spratt S R, Zuurbier R A, Magnant C M and Pennanen M F 1997 Elastography of breast lesions: initial clinical results *Radiology* **202** 79–86
- Horn B K P 1986 *Robot Vision* (New York: McGraw-Hill) pp 278–98
- Kanai H, Hasegawa H, Ichiki M, Tezuka F and Koiwa Y 2003 Elasticity imaging of atheroma with transcutaneous ultrasound: preliminary study *Circulation* **107** 3018–21
- Krouskop T A, Dougherty D R and Levinson F S 1987 A pulsed Doppler ultrasonic system for making noninvasive measurements of the mechanical properties of soft tissue *J. Rehabil. Res. Dev.* **24** 1–8
- Mai J J and Insana M 2002 Strain imaging of internal deformation *Ultrasound Med. Biol.* **28** 1475–84
- Mase G E 1970 Theory and problems of continuum mechanics *Schaum's Outline Series* (New York: McGraw-Hill)
- Maurice R L and Bertrand M 1999 Lagrangian speckle model and tissue-motion estimation—theory *IEEE Trans. Med. Imaging* **18** 593–603
- Maurice R L, Brusseau E, Finet G and Cloutier G 2005 On the potential of the Lagrangian speckle model to characterize atherosclerotic plaques in endovascular elastography: *in vitro* experiments using an excised human carotid artery *Ultrasound Med. Biol.* **31** 85–91
- Maurice R L, Ohayon J, Finet G and Cloutier G 2004a Adapting the Lagrangian speckle model estimator for endovascular elastography: theory and validation with simulated radio-frequency data *J. Acoust. Soc. Am.* **116** 1276–86
- Maurice R L, Ohayon J, Frétygny Y, Bertrand M, Soulez G and Cloutier G 2004b Non-invasive vascular elastography: theoretical framework *IEEE Trans. Med. Imaging* **23** 164–80
- Maurice R L, Pivert N, Daronat M, Qin Z, Foster F S and Cloutier G 2004c Non-invasive elasticity imaging in small vessels: validation on tissue-mimicking phantoms *Medical Imaging 2004, Ultrasonic Imaging and Signal Processing, Proc. SPIE* vol 5373, ed W F Walker and S Y Emelianov (Bellingham, WA: SPIE) pp 184–92
- Ophir J, Céspedes E I, Ponnekanti H, Yazdi Y and Li X 1991 Elastography: a quantitative method for imaging the elasticity in biological tissues *Ultrason. Imaging* **13** 111–34
- SAS IP Inc. 1999 *Ansys Theory Reference* 11th edn
- Weitzel W F, Kim K, Rubin J M, Wiggins R C, Xie H, Chen X, Emelianov S Y and O'Donnell M 2004 Feasibility of applying ultrasound strain imaging to detect renal transplant chronic allograft nephropathy *Kidney Int.* **65** 733–6